Radar-Derived Estimates of Latent Heating in the Subtropics

TINA J. CARTWRIGHT AND PETER S. RAY

Department of Meteorology, The Florida State University, Tallahassee, Florida

(Manuscript received 22 August 1997, in final form 21 May 1998)

ABSTRACT

Atmospheric warming from cloud heating has a major affect on worldwide atmospheric circulations and climate. Studies have shown that the dominant source for cloud heating is the phase change of water. The location and magnitude of cloud heating has a substantial impact on atmospheric circulations. Therefore, identifying the location of phase changes provides information necessary for accurate modeling of atmospheric circulations and climate.

Radar reflectivity is a signature predominantly produced from rain formed from condensation, the primary process that produces heating. Through the application of principal component analysis on a nonhydrostatic cloud model, heating, and derived reflectivity data, a technique to illustrate a future heating algorithm capable of estimating cloud heating from reflectivity data is examined. Formative, intensifying, and mature stages of a Convection and Precipitation Electrification Experiment squall-type convective system were used to demonstrate these results. The accuracy of the technique's estimates for the mean convective and stratiform profiles to within 1.0 K h^{-1} on average throughout the vertical column shows the merit of this statistical technique. The use of this type of technique in conjunction with the network of NEXRAD and spaceborne radars could provide valuable data for applications ranging from cumulus parameterization to 4D data assimilation and model initialization.

1. Introduction

The latent heat released in convection significantly contributes to the dynamics and energetics of large-scale circulations (Simpson 1988; Simpson et al. 1988). This heating arises from water phase changes occurring within strong updrafts and downdrafts that are a part of tropical and extratropical convection. To have an accurate general circulation climate model, it is important to accurately estimate the vertical transport of energy fluxes from the Tropics to the higher latitudes (Riehl and Malkus 1958; Riehl and Simpson 1979) and to accurately place the location and magnitude of the diabatic heating in the vertical plane.

Understanding the vertical distribution of latent heating has become important for global models. Determining this distribution is difficult because heating cannot be directly measured. Heat is initially released by the condensation of water vapor into very small liquid cloud droplets. These droplets grow to 100 μm before they have sufficient terminal velocities to fall as rain. The rain must reach the ground to add a net amount of heat to the air because if the drops remain airborne and evaporate, the condensational heating is balanced by the cooling from the evaporation. The development of techniques that utilize radar to improve the temporal and spatial (horizontal and vertical) estimates of heating as a result of water phase changes due to tropical convection will provide insight into the relationship between heating and precipitation.

This study focuses on the classical squall line convective system with trailing stratiform rainfall (Houze 1993). Although heating profiles are quite variable, general features in the heating/cooling structure of tropical squall line systems can be found throughout the globe. The division that facilitates an easy comparison of characteristic features requires dividing the convective system into its convective and stratiform components. Although convenient to use, some of what is called stratiform contains small convective elements, and some stratiform regions also do not have extensive or easily discernable ''bright bands.'' Within the convective region, the maximum of heating usually exists within the lower troposphere, which is often observed around 2.5 km. Cooling, which is a result of the evaporation of precipitation, may or may not be found near the surface of the convective profile. Within the stratiform region, the maximum heating is found above the freezing level at approximately 7.5 km. At the freezing level, evaporative cooling below changes to condensational/depositional heating aloft.

Three types of studies have yielded information on heating profiles. The first involves observations to estimate the vertical profiles of mass, heat, moisture, and

Corresponding author address: Dr. Peter Ray, Department of Meteorology, The Florida State University, Tallahassee, FL 32306-4520. E-mail: pray@huey.met.fsu.edu

vorticity. The second technique uses models of cumulus ensembles to diagnose the physical mechanisms by which clouds interact with their environment. The third approach uses cumulus parameterization in a model to test the heating budget. Cumulus parameterization is the modeling technique where subgrid-scale cumulus convection is related to the model's scales of motion. In this study, a modification of the second technique is used to examine the role of latent heating within a cumulus ensemble model.

The first technique involves calculations of large-scale energy budgets. Studies on cloud heating have involved the utilization of a network of rawinsondes, which can be used to determine the mean vertical distribution of heating (Yanai et al. 1973; Johnson and Young 1983; Frank and McBride 1989; Chong and Hauser 1990; Gallus and Johnson 1991; Johnson and Bresch 1991; Greco et al. 1994; Halverson et al. 1996). However, the scale of convection is much smaller than the scale of conventional rawinsonde observations. To fill this gap, numerical cloud models have been used to provide detailed information on the microphysical processes, which facilitates explicit calculations of energy budgets on the scale of convection.

Halverson et al. (1996) conducted a diagnostic and modeling study of a mesoscale convective system (MCS) and its heating. They compared the profiles of cumulus heating that were inferred from the sounding observations with those profiles obtained from the cloud-scale energy budgets determined from the Goddard Cumulus Ensemble (GCE) model. The two profiles were similar in both the magnitude and the vertical distribution of heating, which supports the use of cloud model estimations as an important tool for understanding heating and its vertical distribution. In fact, three important heating characteristics were successfully reproduced by the cloud model: the shape of the heating profile, the vertical location of the maximum, and the relative magnitude of heating versus drying (Halverson et al. 1996). The success of Halverson's model simulation provided the rationale for using this particular case study as the focus for this work. The use of both the model-simulated heating and reflectivities provided a validated data source to begin a study on the vertical distribution of heating as related to the convective system structure.

Within the last few years, researchers have begun to examine the problem of insufficient data for the vertical and horizontal distribution of heating/cooling. The hydrometeor/heating algorithm (Tao et al. 1990, 1993) derives cloud heating from vertical hydrometeor profiles. It was developed using the heating and hydrometeor profiles at both the mature and dissipating stages of the cloud system. The algorithm profiles were computed using spatial averages over a 512-km horizontal domain and a 2-h period of time. It successfully reproduces important features that have been obtained from observational studies. The convective-scale heating peaks during the mature period in the lower troposphere near 2.5 km, whereas the stratiform heating peaks near 7.5 km in the mature stage. This algorithm is based on model-derived information such as the vertical hydrometeor profiles, which are quite difficult to obtain directly from observational data.

The second algorithm, the convective/stratiform heating algorithm (Tao et al. 1993), utilizes surface precipitation rates, percentage of stratiform rain, and lookup tables of heating profiles associated with the various cloud systems at different geographic locations. This algorithm was built on the premise that heating profiles associated with squall line systems have many common features once they have been separated into convective and stratiform components. The maximum heating associated with the convective region was found to be in the lower troposphere, whereas the maximum for the stratiform region is in the upper troposphere. The accuracy of this relatively simple algorithm demonstrates the importance of the convective/stratiform classifications.

Section 2 presents a description of the data used by this study including the Convection and Precipitation Electrification Experiment (CaPE) data as well as the GCE model data. Section 3 outlines the methodology of the analysis, which includes the convective and stratiform separation and cell identification routines as well as the application of principal component (PC) analysis to the heating data. Section 4 presents the results as applied to the modeled convective cells, the modeled stratiform cells, and the CaPE observed reflectivity cells. Section 5 summarizes the work and suggests improvements for future research.

2. Overview of data

a. CaPE data experiment

The data used in this study was collected in the CaPE experiment in central Florida on 27 July 1991. This is the same data used by Halverson et al. (1996). The observations used in this study are 1) a 1700 UTC Daytona Beach sounding and 2) radar data from the National Center for Atmospheric Research (NCAR) CP-2 radar. Reflectivity at 2100 UTC composited from multiple National Weather Service WSR-57 radars is presented in Fig. 1. Analysis of a sequence of reflectivity fields provides an overview on the development of the MCS with its convective line and trailing stratiform region. The location of the CP-2 radar is to the northeast of the squall line system. The range height indicator (RHI) cross sections used in this study were collected by this radar. The outline of the Halverson et al. (1996) mesoscale Cross-chain Loran Atmospheric Sounding System sounding network is also shown.

The prestorm environment is depicted in Fig. 2. Halverson et al. (1996) calculated the horizontal divergence from the mesoscale sounding network, which suggests

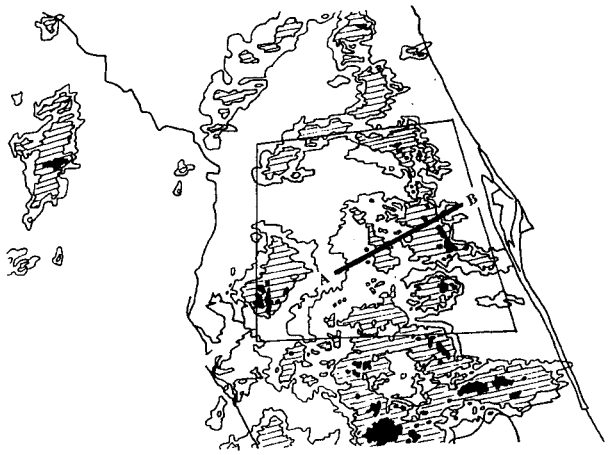

FIG. 1. Composite plan position indicator (PPI) image of developing convection at 2100 UTC 27 July 1991. Rainfall intensity contours correspond to 10 dB*Z* (threshold), 30 dB*Z* (hatched), and 50 dB*Z* (solid black) (Halverson et al. 1996).

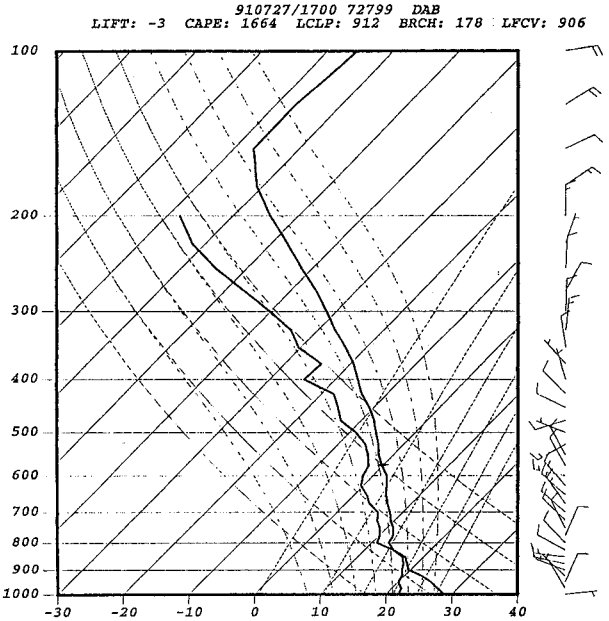

FIG. 2. Skew *T*–log*p* sounding plot of the 1700 UTC Daytona Beach sounding. Wind speeds are shown according to the following convection: half-barb—5 kt, full barb—10 kt (Halverson et al. 1996).

the existence of sea-breeze convergence. The air mass is moderately unstable with a convective available potential energy value of 1664 J kg^{-1}. The environmental winds indicate a weakly sheared environment with northwesterly flow. The cloud system studied was initiated by strong sea-breeze-induced convergence over central Florida at 1700 UTC.

The initial development of convection was associated with the west coast sea breeze. This system then propagated eastward along the west coast sea breeze. By 2100 UTC (Fig. 1), there was further development of a more intense line of convection. This development is attributed to the collision of the east coast sea breeze and the combined west coast sea breeze–gust front. According to Halverson et al. (1996), at approximately 2100 UTC the system reached its mature stage, where it propagated at approximately 6–7 m s^{-1} to the east and began to show signs of patchy stratiform rain west of the leading edge. By 2330 UTC, the area of stratiform precipitation had expanded to the west of the weakening convective line. The system then began to decay and enter its dissipative stage.

This system has the characteristics of a tropical MCS with a convective line and trailing stratiform region (Gamache and Houze 1982; Houze 1989). Halverson et al. (1996) analyzed the CLASS kinematic fields and radar observations and classified the system as evolving through the following stages: undisturbed (1100 and 1400 UTC); genesis of organized deep convection (1700 UTC); squall line maturity (2000 UTC); and dissipation (2300 UTC).

b. Model description

Cloud models provide an invaluable picture of the microphysical interactions within a cloud system. The GCE model is a multidimensional nonhydrostatic dynamic/microphysical cloud model that utilizes a stretched vertical and horizontal coordinate to increase resolution in the lower troposphere (Tao and Simpson 1993). The vertical domain consists of 33 grid points, which are stretched such that the vertical resolution varies from 150 m at the lowest grid point to 1.1 km at the model top, which is at 24 km. The horizontal domain incorporates a central grid domain of 804 grid points with 500-m resolution and an outer domain that is stretched. The total horizontal domain can be up to 674 km wide. The boundary conditions used are open lateral, which allows the normal component of the velocity to exit through the sides of the domain with little reflection. The initial atmospheric conditions vary only as a function of *z*. The model utilizes a 5-km-deep Rayleigh absorbing layer at the model top to dampen vertically propagating gravity waves. The numerical approximations utilized consist of an Arakawa C grid, a leapfrog time approximation, a second-order space derivative in the vertical, and a fourth-order space derivative in the horizontal.

The cloud microphysics contained within the model consist of a parameterized Kessler-type two-category liquid water scheme (cloud water and rain) and a Lin et al. (1983) three-category ice phase scheme (cloud ice, snow, and hail/graupel). Liquid and ice are assumed to be spherical. Size distributions of rain, snow, and graupel (or hail) are taken to be inverse exponential with respect to diameter (D) (Tao and Simpson 1993).

The purpose of this study is to determine a relationship between cloud reflectivity structure and cloud heating. Vertical velocity is found to be important in pro-

viding additional information on cloud structure because it is strongly correlated to cloud heating. Therefore, a complete discussion of the three model parameters is needed.

For diagnostic studies, Yanai et al. (1973) defined the apparent heat source of a large-scale system. The amount of heat, Q_1, is found by horizontally averaging the thermodynamic and water vapor equations. Yanai's equation of Q_1 is the following:

$$Q_1 = \overline{\pi}\left[\frac{\delta\overline{\theta}}{\delta t} + \overline{\mathbf{V}}\cdot\nabla\overline{\theta} + \overline{W}\frac{\delta\overline{\theta}}{\delta z}\right]. \quad (1)$$

In the GCE model, Q_1 is explicitly estimated by the following equation (Soong and Tao 1980; Tao 1983; Tao and Soong 1986; Tao and Simpson 1989):

$$Q_1 = \overline{\pi}\left[-\frac{1}{\overline{\rho}}\frac{\delta\overline{\rho}\overline{w'\theta'}}{\delta z} + \overline{D}_\theta\right] + \frac{L_v}{C_p}(\overline{c} - \overline{e}_c - \overline{e}_r) + \frac{L_f}{C_p}(\overline{f} - \overline{m}) + \frac{L_s}{C_p}(\overline{d} - \overline{s}) + Q_R. \quad (2)$$

The overbars denote horizontal averages, and the primes indicate deviations from the horizontal averages. The variable $\overline{\rho}$ is the density, and $\overline{\pi} = (p/P_{oo})^{R/C_p}$ is the nondimensional pressure, where p is the dimensional pressure and P_{oo} is the reference pressure taken to be 1000 mb. Here C_p is the specific heat of dry air at constant pressure, and R is the gas constant for dry air. The variables L_v, L_f, and L_s are the latent heats of condensation, fusion, and sublimation, respectively. The variables c, e_c, e_r, f, m, d, and s are the rates of condensation, evaporation of cloud droplets and raindrops, freezing of raindrops, melting of snow and graupel/hail, deposition of ice particles and sublimation of ice particles, respectively. The radiative heating/cooling rate is denoted by Q_R. The first term of Eq. (2) on the right-hand side is the vertical eddy heat flux convergence. The subgrid-scale turbulence term is represented by D_θ and is negligibly small compared to other terms (Soong and Tao 1980; Krueger 1988).

The model parameter examined by this study is the microphysical source/sink contribution to heating/cooling at each grid point. As described in Eq. (2), the GCE model contains a total Q_1 term, which is the sum of four contributions: 1) the microphysical sources and sinks (condensation + evaporation + deposition + sublimation + freezing + melting); 2) the vertical eddy flux convergence; 3) the parameterized subgrid-scale diffusion of heat; and 4) radiational heating/cooling. In the case of the CaPE 27 July simulation, radiation was not included in the model physics, so the total Q_1 term is the sum of the first three terms. When grid points are averaged with respect to a large region of the cloud (i.e., convective or stratiform region), the microphysical source/sink term dominates the total Q_1. The eddy flux term is usually less than 10% of the total Q_1 and the diffusion term is also generally small. Because the microphysical term dominates when grid points are averaged, this study examines only this term of the total Q_1.

The model-derived reflectivity is based on the mixing ratios of rain, snow, and graupel/hail. The equations used to calculate the reflectivity values are according to Smith et al. (1975) and Smith (1984) and are related to the inverse exponential drop size distributions of Marshall and Palmer. The rain intercept is 0.08 cm^{-4}; the snow intercept is 0.03 cm^{-4}; and the graupel intercept is 0.0005 cm^{-4}. The density of water is 1.0 g cm^{-3}; the density of snow is 0.1 g cm^{-3}; and the density of rimed ice is 0.9 g cm^{-3}. These density and intercept parameters favor a small number concentration of fast-falling, dense rimed ice particles (i.e., hail), which is consistent with the Lin et al. (1983) ice microphysics scheme.

3. Methodology

Within the model domain, both derived reflectivity and latent heating are calculated by the model. These two variables are known. However, within the observed domain, only the reflectivity is known. Latent heating must then be inferred by applying a derived algorithm devised by this study utilizing the model domain variables. This study utilizes both the model domain's derived reflectivity and latent heating to develop a technique that could be further developed into an algorithm relating the two fields. This same technique can then be applied within the observed domain to the reflectivity field to calculate a corresponding latent heating field.

One way to begin evaluation of the relationship between two variables is to examine a scatter between the two variables. Figure 3a is an example of a scatterplot of each model grid point between latent heating and reflectivity at the mature stage of development of the cloud system. Examination of this plot reveals the complicated relationship between these two variables. Most reflectivity values are associated with no heating. This reflects that processes such as coalescence are occurring as the drops are growing. The peak heating is observed at locations where the reflectivities are approximately 45 dBZ, which is not the peak reflectivity value.

Latent heating results primarily from the condensation of water vapor. The sufficient cooling necessary for condensation could be caused by an updraft lifting an air parcel to higher levels in the atmosphere. Therefore, positive vertical velocity is related to heating. Figure 3b is a scatterplot of latent heating and vertical velocity. In Figure 3b, one relationship between vertical velocity and latent heating can be seen. The strong signal of 0 K h^{-1} heating at all vertical velocities corresponds to the movement of dry air outside the boundaries of the cloud system as well as movement of air with insufficient water vapor to condense. In general, as the vertical velocity increases, the magnitude of latent heating also increases. Likewise, negative vertical velocity (downdrafts) corresponds well with negative heating (cooling).

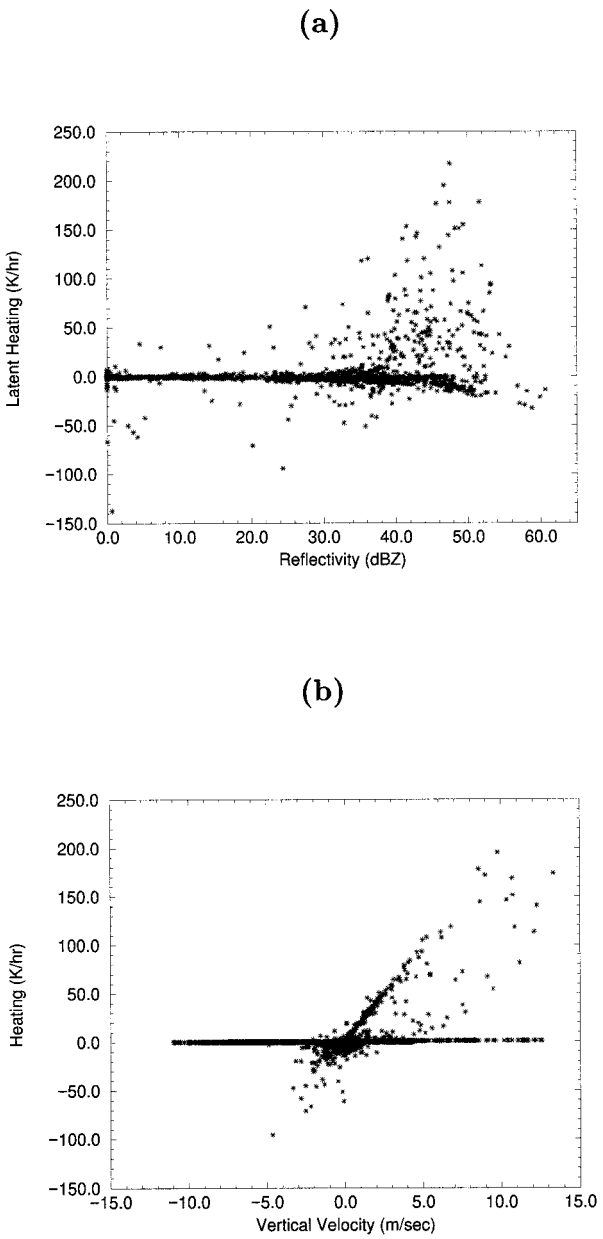

FIG. 3. Scatterplots between (a) latent heating and reflectivity and (b) latent heating and vertical velocity at model time $t = 210$ min at the mature stage of development of the cloud system.

a. Convective and stratiform separation

Certain structural characteristics within a squall-type convective system can be identified utilizing the reflectivity field. These structural characteristics can then be used to infer the strength of the vertical velocity. For example, the kinematics of convective and stratiform regions point to very different vertical velocity fields. Reflectivity can be used to separate the cloud system into convective and stratiform regions and also into organized cells (Steiner et al. 1995).

The fundamental difference between convective and stratiform precipitation regions is their vertical velocity. Stratiform precipitation is defined to exist where the vertical velocity satisfies the condition $|w| \ll |V_t|$, where V_t is the terminal fall velocity of snow particles (1–3 m s^{-1}) (Houze 1993). Convective precipitation, therefore, has vertical velocities that violate the above condition. Incorporating this condition is difficult because of the difficulty in directly measuring vertical velocity. Therefore, much work has been done to differentiate convective and stratiform precipitation based on the horizontal radar echo structure.

The convective/stratiform separation technique used by this study is derived from Steiner et al. (1995). This method incorporates and refines earlier methods developed by Houze (1973), Churchill and Houze (1984), and Steiner and Houze (1993). The method searches for peaks in the reflectivity that satisfy criteria based on the background reflectivity. If the grid points satisfy the criteria, the grid point is labeled as convective. Steiner and Houze (1993) determined the difference between the background and peak to be at least 4.5 dB, which corresponds approximately to the value used by Churchill and Houze (1984). The latest method determines this threshold difference based on the intensity of the central grid point.

The Steiner et al. (1995) study improved on earlier techniques. They added the following criteria: 1) intensity, 2) ''peakedness,'' and 3) surrounding area. A basic threshold is established at 40 dBZ so that any grid point above this value is labeled as convective, since rain of this intensity could practically never be stratiform (Steiner et al. 1995). Those grid points left are labeled convective if their echo is greater than a determined background intensity. This background intensity is determined by the linear average of the nonzero radar echoes within a radius of 11 km around the grid point. For each grid point labeled as convective by the two previous criteria, an area around the central convective grid point is also labeled as convective. The size of this influence area depends on the intensity of the central grid point. For the Steiner et al. (1995) study, the curve that specifies the criteria for establishing the difference above the background intensity is given by the following:

$$\Delta Z = \begin{cases} 10, & Z_{\text{bg}} < 0 \\ 10 - Z_{\text{bg}}^2, & 0 \le Z_{\text{bg}} < 42.43 \\ 0, & Z_{\text{bg}} \ge 42.43, \end{cases} \qquad (3)$$

where Z_{bg} is the background intensity and ΔZ is the difference between the gridpoint value Z and the background intensity Z_{bg}.

For this study, the Steiner et al. (1995) study is adjusted since the reflectivity data are composed of RHI scans. The following procedure is used to identify the classification for each vertical column with a radar echo. First, a threshold test is applied up to a height of 4 km with the threshold equal to 40 dBZ. If a radar echo is found

to be greater than this threshold, the vertical column is set to be convective. The Steiner et al. (1995) gradient classification scheme is then applied to all columns not already found to be convective by the threshold test. First, according to Eq. (3), the difference in Z and Z_{bg}, which must be exceeded for the grid point to be designated as convective, is calculated and applied to the suitable vertical columns. According to Steiner et al. (1995), once a grid point has been identified as convective, surrounding grid points within an intensity-dependent convective radius around that central grid point are also labeled as convective. The following radii are used:

$$\text{Radius} = \begin{cases} 1, & Z_{bg} \le 25 \\ 2, & 25 > Z_{bg} \le 30 \\ 3, & 30 > Z_{bg} \le 35 \\ 4, & 35 > Z_{bg} \le 40 \\ 5, & Z_{bg} > 40. \end{cases}$$

The final step of classification is labeling all the nonconvective vertical columns to be stratiform unless the surface radar echo is less than 5 dBZ, which suggests that this column be labeled as nonsurface precipitating. Thus, echos that may contain imbedded convection, or might be classified as ''other,'' or ''unclassified'' in other taxonomies, are here considered stratiform.

b. Cell identification

In the approach used here, identification of cells helps to isolate the active regions at various stages of development. According to Witt and Johnson (1993), the method used in the WSR-88D cell identification technique searches for connected range gates whose radar echoes are above a specified threshold. This study applies a similar cell identification technique to the model-derived reflectivity field.

For this study, cell identification begins with locating the highest reflectivity value in the cloud system. The value of the highest reflectivity must be greater than 30 dBZ for the technique to classify it as a center of a cell. Two criteria are then used to identify the cell's boundaries. First, if the value of the radar echo is less than 10 dBZ, a boundary has been located. Likewise, if there is a local minimum in radar echo that satisfies a difference threshold with the maximum echo, a boundary has been located. The value of this difference threshold is 25 dBZ. Incorporating this threshold difference criteria facilitated finding cell boundaries even when the reflectivity between cells did not reach less than 10 dBZ. An additional minimum area criteria must also be satisfied for a cell to be identified. The vertical cross-sectional area of the cell must be greater than 10 km^2. Once a pass through the reflectivity field has been completed and all cells have been identified, the final step in the cell identification procedure involves combining cells with similar convective/stratiform classification that have either overlapping vertical boundaries or horizontal boundaries directly connected to one another.

The convective/stratiform classification for a cell is the linear average of all the classified vertical columns found within the cell boundaries. Convective columns are given a value of 2 and stratiform columns a value of 3. All other columns are assigned a value of 0. Therefore, a convective cell is one in which its classification values range from 1.5 to 2.35, whereas stratiform cells range from 2.35 to 3.0. These values were chosen by examining cells and their classification values. Stratiform precipitation can often have embedded convection within its boundaries, which would suggest that columns might be classified as convective while the entire cell should be classified as stratiform. Some examples of the fields of interest with cell boundaries can be seen in Fig. 4. The top two figures are of the reflectivity and heating at the intensifying stage of development, and the bottom two figures are of the reflectivity and heating at the mature stage of development. The thick cell boundaries outline regions identified as convective cells. Likewise, the thin boundaries outline stratiform cells. Overall, the cell identification technique performs quite well in identifying those regions that are most active in the cloud system.

Once all cells and their boundaries have been identified, the final step before PC analysis can begin is the evaluation of the average heating profile for each cell. For each identified cell, the average vertical profile is found by averaging across the horizontal domain for each vertical grid point. Each identified cell has one vertical profile of heating associated with it.

c. Principal component analysis

The PC analysis method is a widely used technique in meteorology because it allows the representation of a large dataset by a much smaller amount of information. The goal of PC analysis is to reduce the dimensions of a dataset by transforming the data to a new set of variables, the principal components. These principal components are uncorrelated and ordered such that the first few represent most of the information in the original dataset. A complete description of PC analysis can be found in Joliffe (1986).

In this study, the primary principal components of the data are extracted to develop representation of the field with high information content. The PC analysis is applied to the vertical profiles of the heating data. Once the PC analysis is complete, physically explaining these primary principal components of the heating profiles and relating them to the reflectivity structure becomes the focus. The first step toward analyzing results is determining the mean profiles of heating for each cell. Throughout the model lifetime of 480 min, each cell identified has an associated heating profile. The accumulation of all of the average heating profiles for each identified cell is the dataset for the PC analysis.

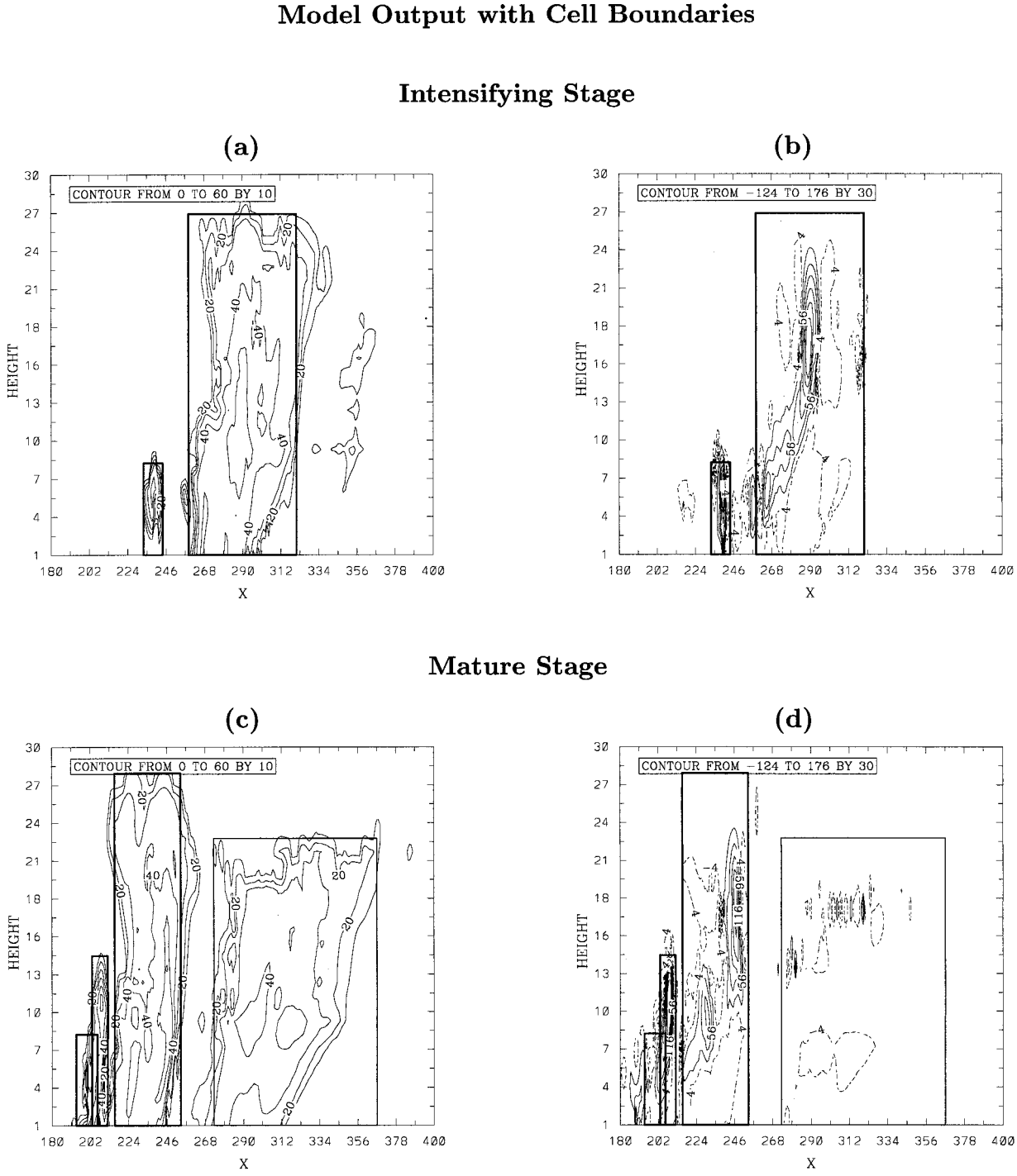

FIG. 4. Model output at two times: (a) and (b) are reflectivity (dBZ) and heating (K h^{-1}), respectively, for model time $t = 150$ min. Similarly, (c) and (d) are the same as (a) and (b) except for model time $t = 213$ min.

1) STATISTICAL VALIDATION OF PC METHOD

The PC method breaks up the data sequence into two parts: the principal components (PCs) and the principal component weights (PCC). The important feature of the PC method is that the original data sequence can be reconstituted utilizing a linear combination of the PCs and the PCC. To verify this application, a sample profile is reconstructed from the linear combination of the first three PCs and the PCC. Mathematically, this can be written as

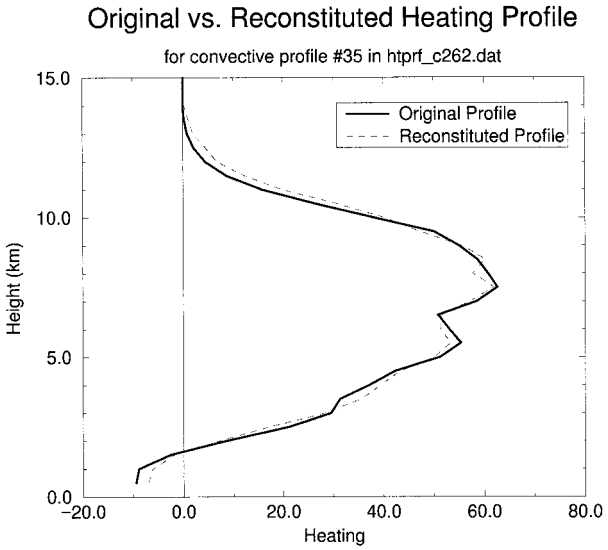

FIG. 5. An original profile of heating data and the reconstituted profile derived from the PC method in units of K h^{-1}.

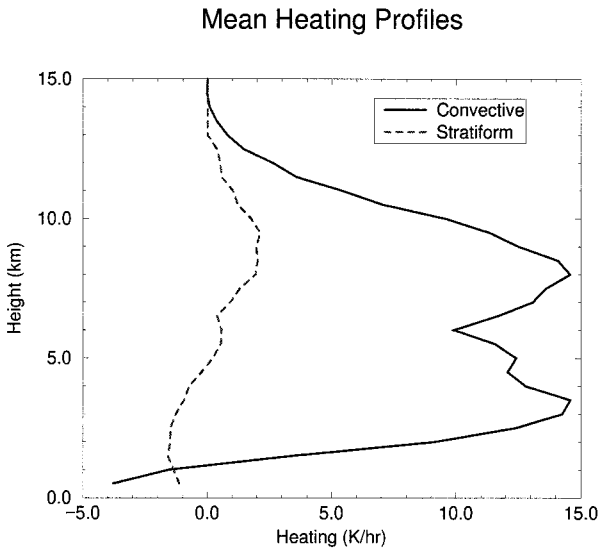

FIG. 6. The computed mean profiles for the convective and stratiform cells.

$$D_n(z) = \mathrm{PC1}(z) \times \mathrm{PCC1}_n + \mathrm{PC2}(z) \times \mathrm{PCC2}_n + \mathrm{PC3}(z) \times \mathrm{PCC3}_n, \quad (4)$$

where D_n represents the sample profile; PC1, PC2, and PC3 represent the first three PCs; PCC1, PCC2, and PCC3 represent the first three PCC; n specifies the number of the particular profile; and z is the variable representing the height. Both the original heating profile and the reconstituted profile are presented in Fig. 5.

2) APPLICATION OF PC METHOD

The relationship between heating and reflectivity is not a direct relationship. The processes are connected because cloud water generally forms by condensation, which generates most of the cloud heating, and a reflectivity signature results from the coalescence and growth of cloud water into raindrops. The goal of this research is to examine what relationship exists between the condensation heating and the observed rain. Applying the PC analysis to the dataset reveals promising results. For the heating data, the first three PCs explain approximately 91% of the total variability for the convective cells and 80% of the total variability for the stratiform cells.

The PC analysis is applied to the convective and stratiform cells separately. Separation of the analysis into convective and stratiform cells is beneficial because different microphysical processes are important within each type of cell. For both classifications, 80% of the heating profiles are separated into a training dataset so that 20% of the model data could be used as a testing dataset independent of the training dataset. Every fifth profile is set aside into the testing dataset for an independent analysis of the quality of the technique.

It must be noted that when examining the PCs and PCC for heating, each PC is the variability to the mean profile. Even when the PC has a value of zero, there is still heating/cooling associated with the mean heating profile. The mean heating profiles for both the convective and stratiform cells are included in Fig. 6. Clearly, most heating takes place in cells classified as convective.

(i) Convective analysis

The three PCs calculated for the training dataset of 206 convective heating profiles are located in Fig. 7. The first PC is noted by the heavy solid line. It explains

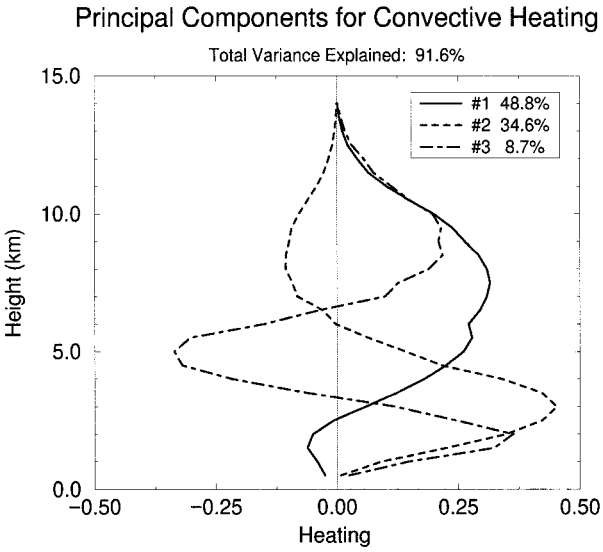

FIG. 7. The three primary principal components (PCs) for convective heating derived from the PC method.

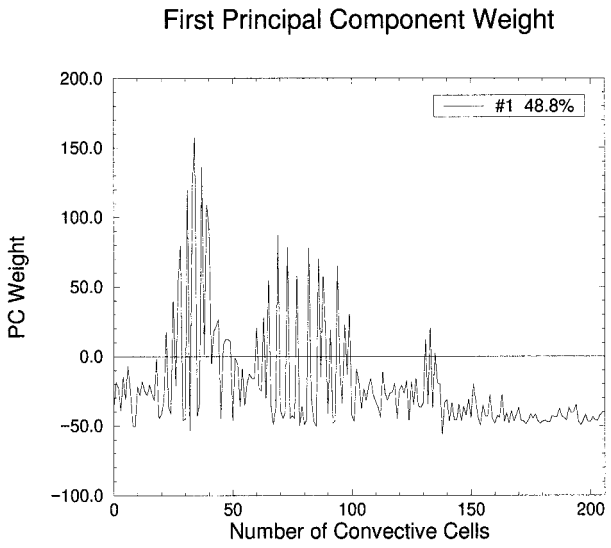

FIG. 8. The first component weight (PCC) for convective heating derived from the PC method.

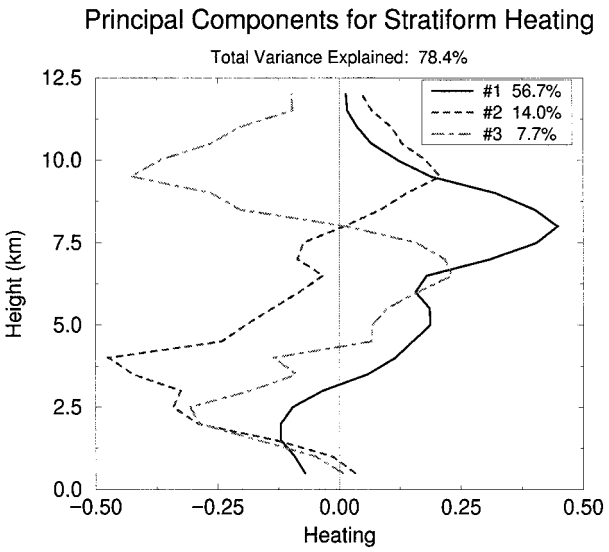

FIG. 9. The three primary PCs for stratiform heating derived from the PC method.

nearly 50% of all the variability. This profile is similar to the characteristic profile suggested by Houze (1982). A strong relative maximum is found in the middle troposphere at about 7 km. At the surface, there is a weak crossover to cooling, which results from the evaporation of precipitation. The second and third PC are also presented in Fig. 7. The second profile is related to shallow new convection with a lower-tropospheric heating maximum. These additional PCs also help explain the small degree of variability to the characteristic profile that is seen for a particular profile.

Each PC has a corresponding PCC that contains the fluctuations of the PC over the length of the model simulation. The PCC associated with the first PC is shown in Fig. 8. Examination of this plot reveals the complexity of the variations of the PCC for the convective cells. This complexity arises from the way the cells are extracted and entered into the total convective cell dataset. For a single model output time, each identified convective cell may be at different stages of convective development, which results in sharp fluctuations of the PCC. The second and third PC have corresponding PCC, which look similar to the one shown in Fig. 8.

(ii) Stratiform analysis

The three PCs calculated for the training dataset of 64 stratiform heating profiles are shown in Fig. 9. The total number of stratiform heating profiles is much less than the identified convective heating profiles because there are far fewer stratiform cells identified in the model simulation. Because of the fewer number of profiles in this dataset, the PCs appear to be less refined than in the convective case. The first PC is noted by the heavy solid line. It explains nearly 57% of all the variability and resembles the characteristic profile suggested by Houze (1982). There is a strong cooling maximum in the lower troposphere at about 1.5 km and a heating maximum in the upper troposphere at about 8 km. The crossover from cooling to heating occurs near the freezing level located around 3 km. The cooling at the surface is a result of the partial evaporation of falling precipitation. The second and third PCs are also presented in Fig. 9. These additional PC contribute the small variability to the principal PC found for certain stratiform cells.

d. Multiple-linear regression analysis

The PC analysis is done by examining the training dataset of mean vertical heating profiles for the identified convective and stratiform cells. Through this statistical analysis, the most important vertical heating profiles are determined and can be physically explained. These are the PC profiles found in Figs. 7 and 9. Explanation of the PCC that correspond to each convective and stratiform PC is more difficult because they are dependent on how the PC varies over time. Therefore, the PCC must be related by multiple-linear regression analysis to identifiable structural characteristics from the derived reflectivity field, for example, the area of the cell and the computed total water mass from the reflectivity found within a cell. Because of the limitations of the observed reflectivity scans, this method is designed to work on single reflectivity scans so only those relevant instantaneous structural characteristics were examined.

A list of the structural characteristics and the respective relative percentage weight explaining each PCC is given for the convective cells in Table 1 and for the stratiform cells in Table 2. The total percentage ex-

TABLE 1. The relative percentage contributions to each PCC by different structural characteristics for the convective cells.

Structural characteristics	1st PCC	2d PCC	3d PCC
Total water mass	56.5	0.7	
Area	22.3		
Aspect ratio		1.7	
Distance to the leading edge	0.4	29.1	1.8
Maximum reflectivity	0.4	8.5	1.4
Surface rain rate	0.3		
Height of cell	3.0	10.3	4.3
Bottom of cell	0.3	2.5	
Total	84.1%	56.6%	8.3%

TABLE 2. The relative percentage contributions to each PCC by different structural characteristics for the stratiform cells.

Structural characteristics	1st PCC	2d PCC	3d PCC
Total water mass	30.6		3.4
Area	26.2	41.7	
Aspect ratio	4.4		
Classification	6.9	2.6	
Maximum reflectivity		12.7	
Surface rain rate		17.0	17.4
Height of cell	4.7		
Bottom of cell	1.7		35.0
Total	74.5%	74.0%	55.8%

plained for each PCC is less than 100%. However, a linear combination of the terms shown in Table 1 explains nearly 85% of the first PCC for the convective cells and nearly 75% for the stratiform analysis. These total percentages explained allow the most important PCC, the first few, to be reconstituted with a fair amount of accuracy.

Certain structural characteristics are found to be more important in reconstructing each of the PCC for both convective and stratiform cells. The most important structural characteristics are those with the largest values of the percentage explained. The first PCC for both the stratiform and convective cells is primarly explained by the total water mass found within the cell boundaries and the area of the cell. Water mass values are directly correlated with reflectivity values. Therfore, cells with a high water mass term have an intensification in their heating/cooling. Physically, the area of the cell is connected with the size of the cell, which suggests that the larger the cells the lower the overall magnitude of heating/cooling. Small, intense convective cells have higher heating values than larger, older convective cells. For the second PCC in the convective analysis, the distance to the leading edge term explains the majority of this PCC and can be physically connected to the age of the cell. Young, intense convection is situated at the leading edge and has very intense heating values. Likewise, older and weaker convection has a nonzero distance term and weaker heating values. In a similar manner, the other important terms for the primary PCC have strong physical connections to the distribution of heating found within the cells.

4. Results

Analysis of the technique's accuracy relies on examining the heating profiles derived for the testing dataset for both convective and stratiform cells. There were 51 testing profiles for the convective classification and 16 profiles for the stratiform classification that cover the range of cloud development.

a. Convective cells

The first comparative analysis for the convective test cases was on the averaged total heating profile for all 51 test profiles shown in Fig. 10. The original profile is the model heating profile for all the convective testing dataset, and the reconstituted profile is the derived heating profile found for each convective cell within the convective testing dataset. The agreement between the model output and the derived profiles is quite good. The rmse between the two profiles is 0.91 K h^{-1}, which is quite good when the maximum heating is 17 K h^{-1}.

The technique clearly performs well for the computed average profiles, but evaluation for each convective profile can be made. The total heating for each convective profile, which was computed as the area under the curve of the heating profiles for both the model profiles and the estimated profiles, is presented in Fig. 11. The technique fairly accurately estimates the total heating and/or cooling for most convective cells. The standard rmse were computed for all 51 test profiles. The values range from 1.8 K h^{-1} to 18.7 K h^{-1}. The average rmse was

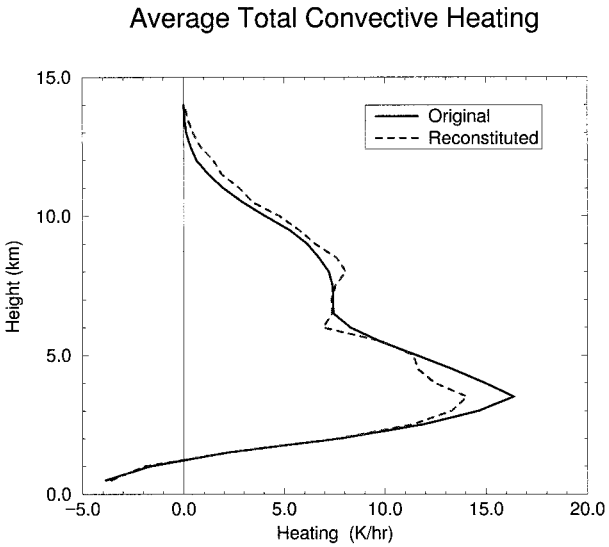

FIG. 10. The averaged total heating from all the testing dataset convective heating profiles in units of K h^{-1}.

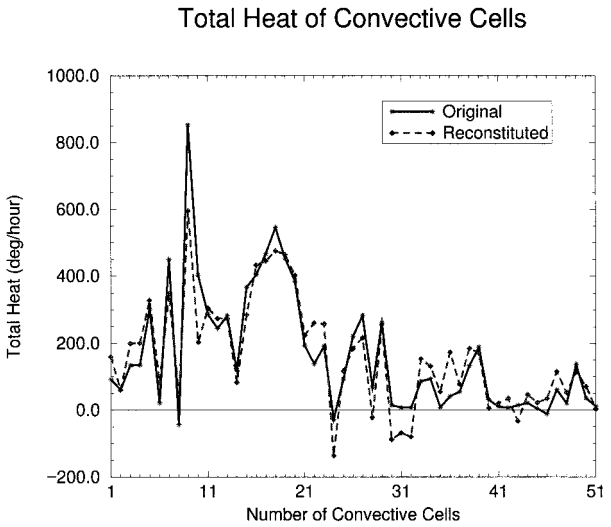

FIG. 11. Comparison of the total heating found for each convective cell of the original model heating profiles and the derived profiles in units of K h^{-1}.

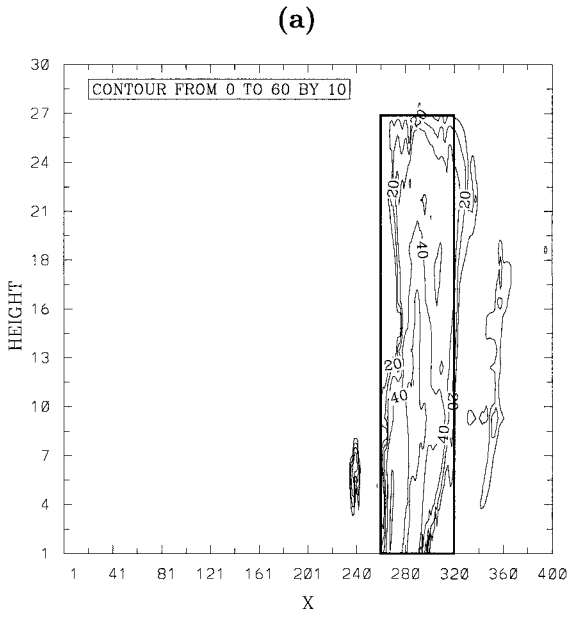

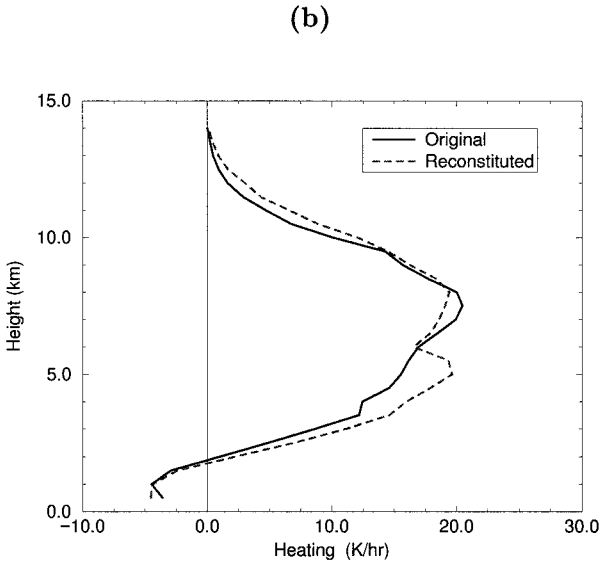

FIG. 12. The (a) model-derived reflectivity field (dBZ) and (b) heating profiles (deg h^{-1}) for model output time of 147 min for cell number 1.

computed as 6.2 K h^{-1}, which is more than the rmse computed for the total average heating profile. This suggests that some of the errors due to overestimating the heating are compensated for by underestimates in other profiles in the ensemble average profile.

Through the examination of profiles where the accuracy is both high and low, analysis can be made on the strengths and relative weaknesses of the technique. The lowest rmse are found in profiles 12 and 14, which both correspond to mature convective cells as shown for profile 12 at model output time 147 min in Fig. 12a. The model and the reconstituted profiles are shown in Fig. 12b. The rmse between the two profiles is 1.8 K h^{-1}. The total heating, which is the area under the heating profile curve, for the model data is 245 K h^{-1} and that for the reconstituted profile is 274 K h^{-1}, which is a difference error of 12%. Both profiles 12 and 14 correspond to this same type of cell with similar heating profiles. The technique does quite well in correctly analyzing the heating for these mature convective cells.

The greatest rmse were found for profiles 21 and 22 with values near 18 K h^{-1}. Examination of both the reflectivity and heating profiles can help explain why the technique failed to perform well with rmse an order of magnitude larger than the previous cells. Profiles 21 and 22 correspond to cell numbers 3 for model output times 207 min and 210 min. The cell boundaries identify only the front half of the mature convective cell to be specified as a cell. This error is a result of the way the boundaries of cells are identified. If a local maximum exists that is not associated with the center of a cell, cell boundaries can be misplaced. For this cell, the model and reconstituted profiles clearly do not agree on the heating characteristics of this cell. However, moving the cell boundaries to correctly reflect the true boundaries of the cell corrects this problem. The new rmse between the model and reconstituted profiles dramatically decreased to 4.1 K h^{-1}.

The other large rmse exist for profiles 9 and 10 with rms values near 16 K h^{-1}. These profiles correspond to model output times 117 min and 123 min, respectively. The cell for model output time 117 min is the first truly mature cell to develop to a height of 13 km. This technique appears to have problems resolving the intense heat generated within such an intensely maturing cell. The total heating rate found with the model heating is 853 K h^{-1}, whereas the technique estimates only 594

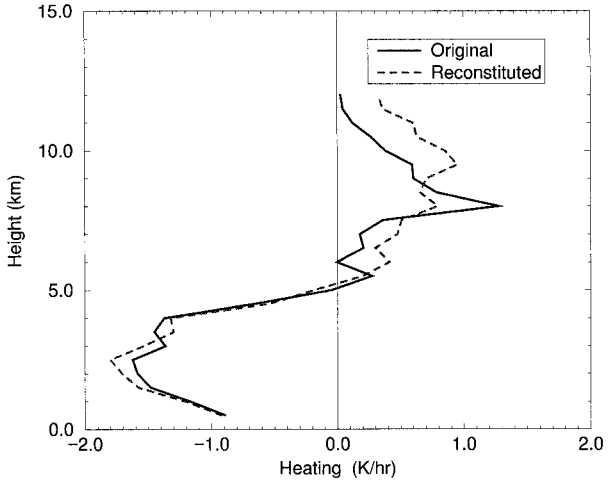

FIG. 13. The averaged total heating from all the testing dataset stratiform heating profiles in units of K h^{-1}.

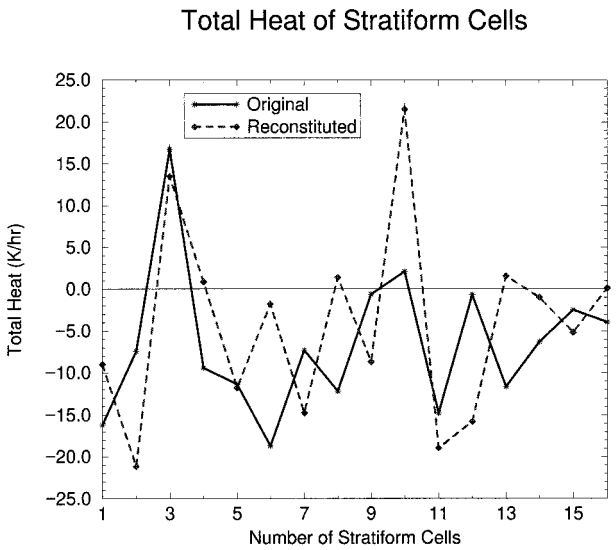

FIG. 14. Comparison of the total heating found for each stratiform cell of the original model heating profiles and the derived profiles in units of K h^{-1}.

K h^{-1} to be the total heating rate, which is a 30% difference. Similarly, the cell for model output time 123 min is a very intense developing cell that reaches a height of only 6 km. The total heating rate with the model is 403 K h^{-1}, whereas the technique estimates only 204 K h^{-1}, which is a 50% error. This degree of error is a result of the initiation of intense convective activity that the technique cannot adequately resolve. This error results because such heating intensities occur so infrequently that the technique statistics cannot adequately resolve them. In other words, the training dataset does not support enough examples of these intensely convective cells.

Overall, the technique does quite well in estimating the magnitude of maximum heating, the location of that maximum, the presence of evaporative cooling at the surface, and the total heating for these convective cells. In general, the errors between the model and derived profiles result from the need for automation of identification of cell characteristics such as cell boundaries and classifications. This need and desire for automation should be reevaluated to ensure the most accurate estimations of vertical heating.

b. Stratiform cells

Because of the structure of cloud systems, a mature or dissipative cloud system can have multiple convective regions but only one mature stratiform region. Therefore, fewer stratiform cells are available to be used as a dataset than convective cells. In fact, only 80 stratiform cells were identified throughout the entire model run, which allows only 16 stratiform cells to be used as a testing dataset. The first comparative analysis for the stratiform test cases was on the averaged total heating profile for all 16 test profiles shown in Fig. 13. The original profile is the model heating profile for all of the stratiform testing dataset, and the reconstituted profile is the derived heating profile found for each stratiform cell within the stratiform testing dataset. The agreement between the model output and the derived profiles is good. The rmse between the two profiles is 0.26 K h^{-1}.

Another comparison can be made between mature and dissipative stratiform cells. Because the development of stratiform cells typically follows the overall trend of development of the entire cell, mature stratiform cells were identified from model output times 225 min through 297 min. The averaged ensemble heating profile for the mature stratiform cells was computed. The rmse between the model and derived profile is 0.42 K h^{-1}, which is higher than the total average profile. An average ensemble heating profile was computed for the dissipative stratiform cells that were identified between model output times 306 min and 396 min. The rmse between the model and derived profile is 0.33 K h^{-1}, which is higher than the total averaged profiles but less than the averaged mature stratiform profile. This suggests that the technique does better for the dissipative cells than the mature cells. However, the technique does quite well in locating the evaporative cooling maximum in the lower troposphere and the heating maximum in the upper troposphere above the freezing level.

The technique does well for the computed average profiles, but assessment can be made for the level of accuracy for each testing dataset stratiform profile. The total heating for both the model profiles and the estimated profiles is presented in Fig. 14. The technique fairly accurately estimates the total heating and/or cooling for most stratiform cells. Comparing the magnitudes of total heating for the stratiform cells, in Fig. 14, and the convective cells, in Fig. 11, reveals that the convective cells have much more heating than the stratiform

cells. Because convective cells have much higher heating rates, estimations of the vertical heating of convective cells tend to be more important than estimations made for the stratiform cells. However, stratiform cells can contribute toward the total heating if the stratiform area is large. This technique merely shows that this method might be a viable alternative for estimating heating profiles.

The standard rmse were computed for all 16 test profiles. The values range from 0.8 K h^{-1} to 1.5 K h^{-1}. The average rmse was computed as 1.0 K h^{-1}, which is more than the rmse computed for the total average heating profile. This suggests that the errors are being reduced as more cells are combined to form an ensemble average profile. The magnitudes of the rmse for the stratiform cells are much lower than the rmse for the convective cells. Again, this is a result of the differences in the magnitudes of heating in convective and stratiform cells.

From Fig. 14, the testing stratiform cell with the most heating occurs at profile number 3, which corresponds to cell number 3 at model output time 255 min shown in Fig. 15. The maximum heating in the original profile is 7.4 K h^{-1} and the maximum heating for the derived profile is 4.8 K h^{-1}. The technique does very well in identifying the location and the magnitude of the cooling below the freezing level. However, the slight misrepresentation of the magnitude of the maximum heating and its location yields an rmse of 1.2 K h^{-1}. The values of the model and estimated total heating are 16.7 K h^{-1} and 13.5 K h^{-1}, respectively, which corresponds to an error of 19%.

c. *Real reflectivity data*

The final step in analysis is the application of this heating estimate technique to the observed reflectivity data from the CP-2 radar. Latent heating can be inferred for the observable domain through the application of the heating estimate technique. Discussion will include the inferred latent heating for three reflectivity scans corresponding to the formative, intensifying, and mature stages of development of a cloud system. The following RHI scans were all taken along the 231° radial from the CP-2 radar location close to Kennedy Space Flight Center (KSFC) so that development can be sufficiently monitored along the same path.

The first two stages of development consist of the formative and the intensifying stages. For the formative stage of development, Fig. 16a depicts the observed reflectivity for the RHI scan at 2105 UTC. Development is occurring in isolated cells with one convective cell outlined. The derived heating is shown in Fig. 16b. The total heating resulting from this formative cell is 225 K h^{-1}. For the RHI scan at 2130 UTC, an intensifying convective cell is depicted in Fig. 17 where (a) is the observed reflectivity and (b) is the derived heating. The isolated cells have begun to merge and grow in intensity.

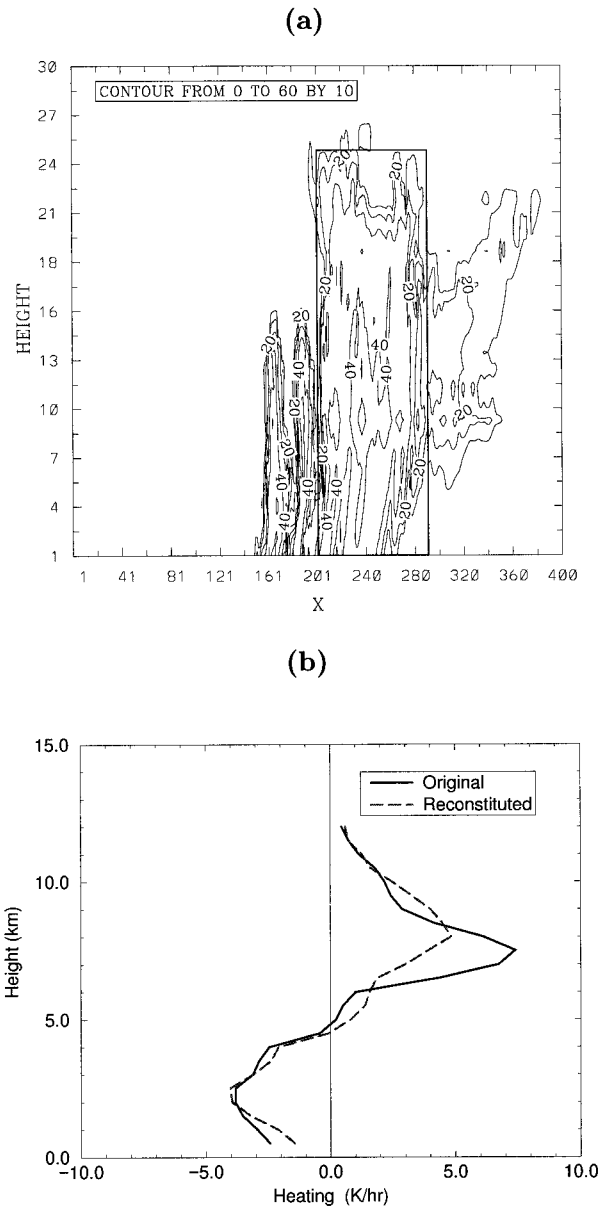

FIG. 15. The (a) model-derived reflectivity field (dB*Z*) and (b) heating profiles (K h^{-1}) for the stratiform cell at model output time of 255 min for cell number 2.

The total heating resulting from the derived heating profile for this intensifying cell is 163 K h^{-1}.

For both the formative and intensifying convective cells, the heating profiles look close to anticipated values. The location of the elevated heating maxima at around 8 km agrees well with modeled heating. However, the formative cell heating exhibits more cooling at the surface than the model profiles. One explanation could be that the heights of the observed convective cells are consistently taller than in the model. For this technique, the height of the cell is an important term governing the magnitude of low-level heating. The

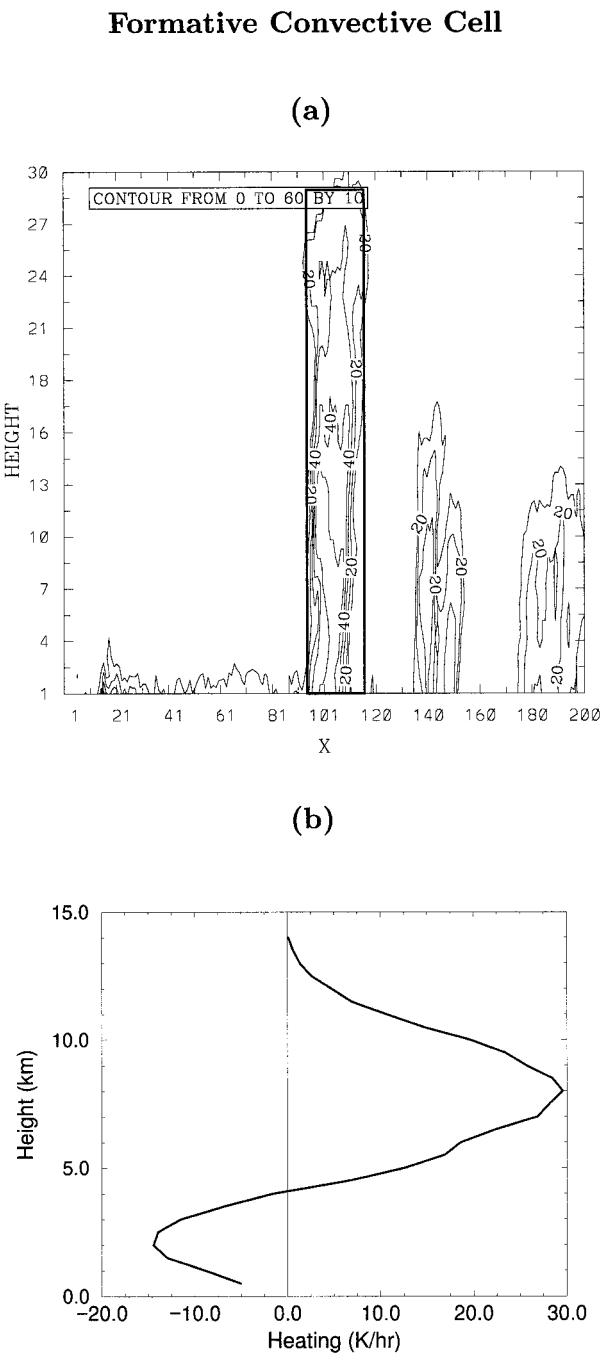

FIG. 16. The (a) reflectivity field (dBZ) and (b) derived heating profile (K h^{-1}) for the cell at 2105 UTC at 231°.

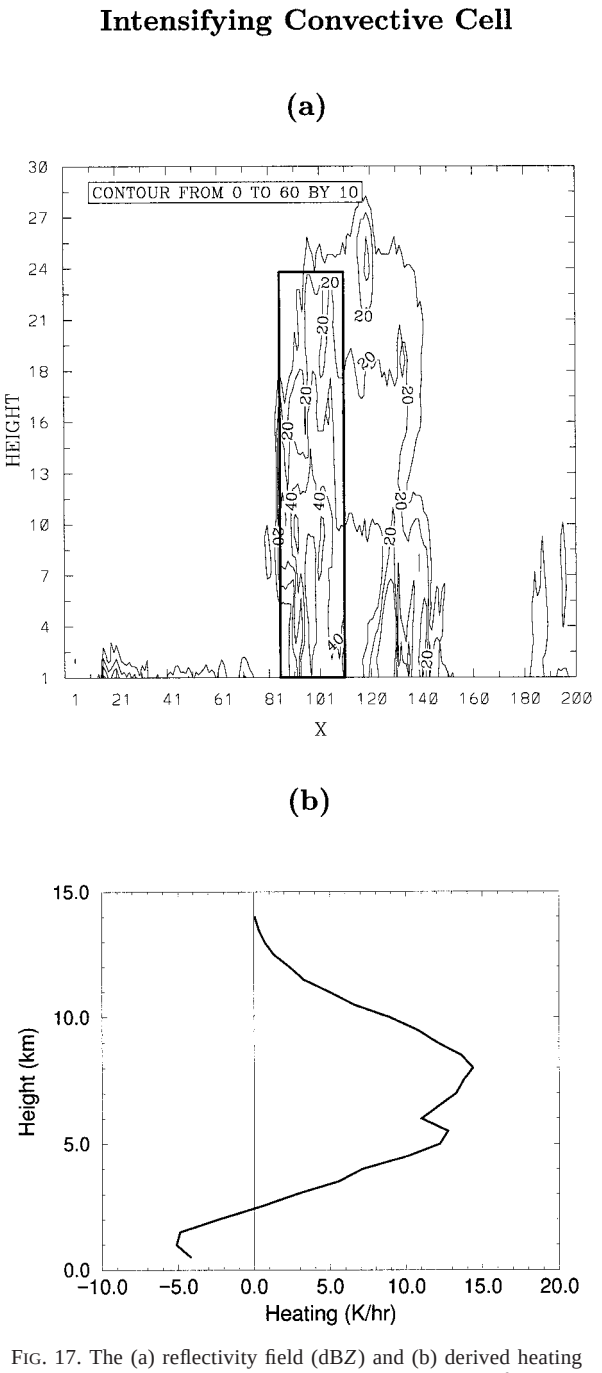

FIG. 17. The (a) reflectivity field (dBZ) and (b) derived heating profile (K h^{-1}) for the cell at 2130 UTC at 231°.

shorter the cell, the more the heating maximum is lowered. Likewise, the taller the cell, the more the heating maximum is raised. For the formative convective cell, the height of the cell is 14.5 km, which results in a derived deep layer of surface cooling. The values of the total heating appear to be less than what was found in the model data for formative and intensifying cells. An explanation could be that the modeled reflectivities appear to be higher than the observed reflectivities. The total water mass computed from reflectivity is the primary factor determining the weight on the first PC. Looking at Fig. 7, the first PC determines the maximum heating to occur at 8 km. High reflectivities result in high total water mass, which gives a large weight to the first PC and the 8-km heating maximum. With lower observed reflectivities, the total heating will therefore be lower than the modeled total heating.

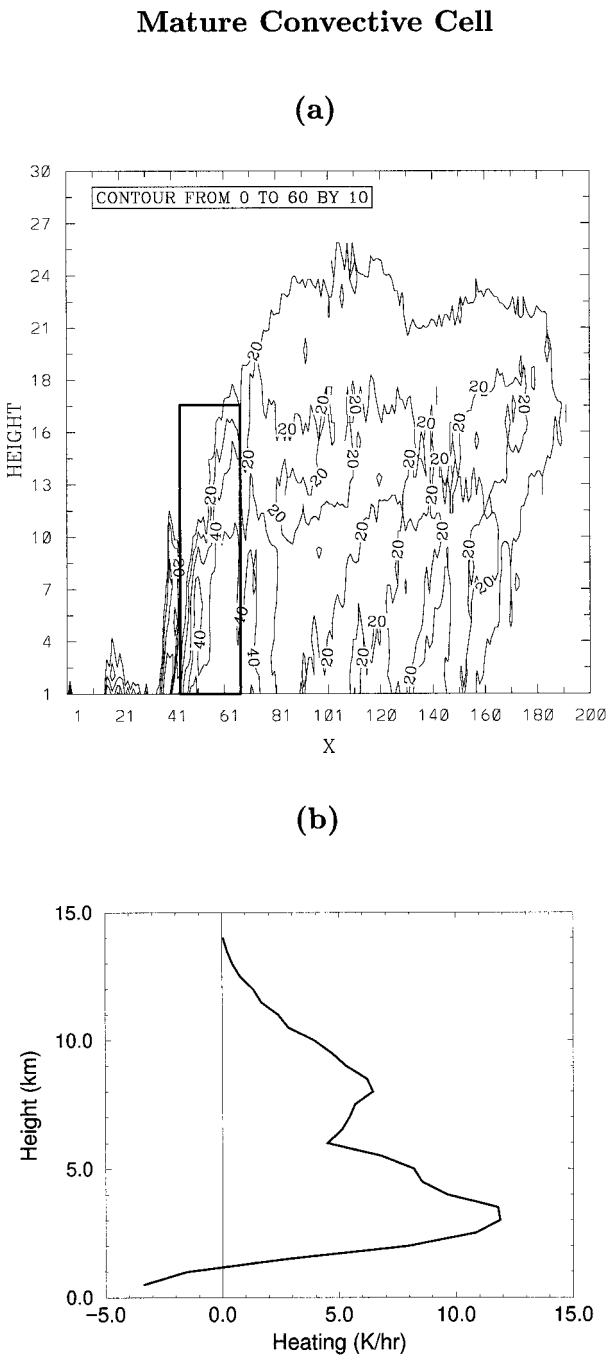

FIG. 18. The (a) reflectivity field (dBZ) and (b) derived heating profile (K h^{-1}) for the convective cell at 2230 UTC at 231°.

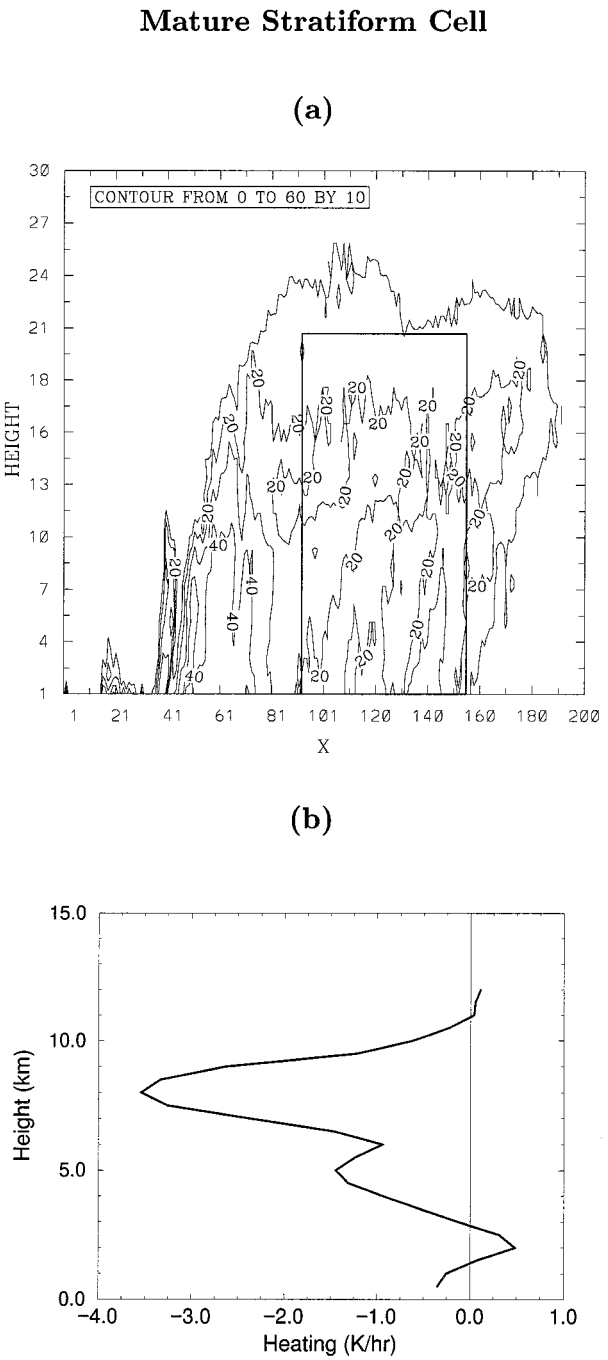

FIG. 19. The (a) reflectivity field (dBZ) and (b) derived heating profile (K h^{-1}) for the cell at 2230 UTC at 230°.

A mature cell is depicted in Figs. 18 and 19 at 2230 UTC where the cells have merged and have formed a well-organized stratiform region behind the leading edge of convection. For the convective cell, Fig. 18a depicts the observed reflectivity, and the derived heating is shown in Fig. 18b. The total heating resulting from the derived heating profile for this convective cell is 130 K h^{-1}. The well-developed mature stratiform region that has formed behind the leading edge of convection is depicted in Fig. 19a. Figure 19a depicts the observed reflectivity, and the derived heating is shown in Fig. 19b. The total heating resulting from the derived heating profile for this stratiform cell is -25 K h^{-1}.

Several features can be discussed for these two mature profiles. The heating profile for the mature convective cell agrees well with our conceptual model. The double

heating maximum seen in Fig. 18 exists within cells that have both a relatively low height and sufficient reflectivities to generate a large total water mass. According to the diagram for the convective PCs and the previous discussion, the first and second PC weights can support two maxima in the reflectivities. However, the stratiform profile does not match well with any of the model profiles. The stratiform cells have lower reflectivities in the observed data than in the model. From the linear regression results on the stratiform analysis in Table 2, the term with the most importance for the first PC is the total water mass. With lower reflectivities, the total water mass is lowered, which will affect the derived heating profile. An additional point regarding the stratiform analysis is the number of modeled stratiform cells. Because of the fewer number of stratiform cells than convective cells, the technique statistics will be less stable for the stratiform analyses than for convective analyses. This problem can be solved through the incorporation of multiple model runs involving stratiform precipitation.

5. Conclusions

A technique that offers future possibilities as a heating algorithm has been developed to estimate diabatic heating from reflectivity patterns observed by radar. The technique was established and tested on a nonhydrostatic cloud model simulation of a CaPE squall-type convective system. Both identified structural characteristics and diabatic heating are used as inputs into a combined PC and multiple-linear regression analysis. Cell identification and convective/stratiform cell classification of the reflectivity data serves to isolate and classify regions of active precipitation. Once the active cells have been identified, structural characteristics such as cell height, total water mass within the cell, etc., are used along with the statistical analysis results to estimate diabatic heating. Once the statistical analysis on the model data was completed, observed reflectivity data was used to obtain the structural characteristics needed to obtain the estimated diabatic heating.

The accuracy of the technique was tested by examining 20% of the model data, which were designated as the testing dataset and separated from the training dataset used to establish the statistics. The results from the application of the technique to the testing dataset are encouraging. The estimates of the diabatic heating closely resemble the model outputs of heating. For the testing dataset, the technique estimates the magnitude of diabatic heating for the mean convective and stratiform heating profiles to within 1.0 K h^{-1} on average throughout the vertical column. The errors are higher on estimations of instantaneous rates for individual profiles. However, vertical distributions of heating for the entire system were estimated with errors less than 0.91 K h^{-1} for the convective region and 0.26 K h^{-1} for the stratiform region.

Application of the technique to real reflectivity data was the final step in this study. Because of the structure of the CaPE experiment, continuous radar coverage of the squall line does not exist. Therefore, the technique can be applied only to a few RHI scans taken of the squall line system. Only instantaneous rates of diabatic heating can be obtained with this small amount of radar data. These instantaneous rates compare well with modeled instantaneous rates of heating.

Direct comparison between the magnitudes of the heating profiles derived for this case by Halverson et al. (1996) and the technique is difficult. The low number of radar scans means the technique could not be applied over the same time and space domain covered by Halverson's work. Halverson's estimates are based on sounding observations taken at 3-h intervals. This technique identifies and confines the examination to only those active precipitation and heating regions. One important comparison can be made with Halverson et al.'s (1996) work. Comparisons of the general vertical distribution of heating can be made because inclusion of nonactive precipitating regions will decrease only the magnitude of the heating and not change the shape of the profile. Both profiles agree on the height of the heating maximum as well as the presence of evaporative cooling at the surface.

Previously derived heating algorithms rely upon look-up tables or hydrometeor profiles that are difficult to measure and obtain for global applications. Comparisons between the accuracy of the algorithms are difficult. First, the hydrometeor-heating algorithm relies on data that is undesirable for an observational technique. Second, the temporal and spatial resolution of both the previously derived algorithms differs significantly from the proposed technique making direct comparison difficult. The accuracy of the proposed heating technique is difficult to be compared with previous algorithm accuracy because of the differences in the spatial and temporal resolution. However, the relative accuracy of this technique reveals that this combined statistical modeling and observational technique could be examined further for better heating profile estimations.

The accuracy of the heating estimations of this technique have demonstrated the possibility of establishing a statistical technique to determine a relationship between radar reflectivity and cloud heating. An improved version of this type of technique would be well suited for spaceborne radars such as the precipitation radar to be on the Tropical Rainfall Measuring Mission (TRMM) satellite because of the satellite sampling rate. This technique was built on estimating instantaneous heating from reflectivity scans. The sampling rate of the precipitation radar will be such that these type of estimations will be most accurate. This heating technique has provided new insight into the possibilities of utilizing radar reflectivity to estimate heating. Before this technique can be adequately tested on a global scale, several improvements should be made. Incorporating more

modeling studies in the statistics would increase overall stability of its application to various types of convective systems. Also, incorporation of different cloud models and their simulations would help remove the technique's dependence on one cloud model's results. Overall, the use of the cloud model simulation and the application of observed radar reflectivity has shown that this technique has both the capability to estimate cloud heating and the promise of providing data for cumulus parameterization, four-dimensional data assimiliation, and model initialization.

Acknowledgments. Special appreciation is extended to the cloud modeling group at Goddard Space Flight Center, including Dr. W.-K. Tao, Mr. Stephen Lang, and Dr. Jeff Halverson, who have provided much valuable information used by this study, and to Mr. David Wolff and the TRMM Ground Validation group at GSFC for their help and support. Appreciation should also be given to Mr. Bret Whissel for computing support. Thanks must be given to the National Physical Science Consortium as well as NASA Goddard Space Flight Center, who provided the financial support to one of us (T. J. Cartwright) to pursue this research. Partial support for this research was provided by NASA Grant NAG5-2719 (TRMM) and NOAA Grants NA57RA0482 (southeast consortium) and NA37WA0361 (CITM).

REFERENCES

Chong, M., and D. Hauser, 1990: A tropical squall line observed during the COPT 81 experiment in West Africa. Part III: Heat and moisture budgets. *Mon. Wea. Rev.*, **118,** 1696–1706.

Churchill, D. D., and R. A. Houze Jr., 1984: Development and structure of winter monsoon cloud cluster on 10 December 1978. *J. Atmos. Sci.,* **41,** 933–960.

Frank, W. M., and J. L. M. McBride, 1989: The vertical distribution of heating in AMEX and GATE cloud clusters. *J. Atmos. Sci.*, **46,** 3464–3478.

Gallus, W. A., and R. H. Johnson, 1991: Heat and moisture budgets of an intense mid latitude squall line. *J. Atmos. Sci.*, **48,** 122–146.

Gamache, J. F., and R. A. Houze Jr., 1982: Mesoscale air motions associated with a tropical squall line. *Mon. Wea. Rev.*, **110,** 118–135.

Greco, S., J. Scala, J. B. Halverson, H. L. Massie Jr., W.-K. Tao, and M. Garstang, 1994: Amazon coastal squall lines. Part II: Heat and moisture transports. *Mon. Wea. Rev.*, **122,** 623–635.

Halverson, J., M. Garstang, J. Scala, and W.-K. Tao, 1996: Water and energy budgets of a Florida mesoscale convective system: A combined observational and modeling study. *Mon. Wea. Rev.*, **124,** 1161–1180.

Houze, R. A., Jr., 1973: A climatological study of vertical transports by cumulus-scale convection. *J. Atmos. Sci.*, **30,** 1112–1123.

——, 1982: Cloud clusters and large-scale vertical motions in the Tropics. *J. Meteor. Soc. Japan*, **60,** 851–859.

——, 1989: Observed structure of mesoscale convective systems and implications for large-scale heating. *Quart. J. Roy. Meteor. Soc.*, **115,** 425–461.

——, 1993: *Cloud Dynamics.* Academic Press, 573 pp.

Johnson, R. H., and G. S. Young, 1983: Heat and moisture budgets of tropical mesoscale anvil clouds. *J. Atmos. Sci.,* **40,** 2138–2147.

——, and J. F. Bresch, 1991: Diagnosed characteristics of precipitation systems over Taiwan during the May–June 1987 TAMEX. *Mon. Wea. Rev.*, **119,** 2540–2557.

Joliffe, I. T., 1986: *Principal Component Analysis.* Springer-Verlag, 271 pp.

Krueger, S. K., 1988: Numerical simulation of tropical cumulus clouds and their interaction with the subcloud layer. *J. Atmos. Sci.*, **45,** 2221–2250.

Lin, Y.-L., R. D. Farley, and H. D. Orville, 1983: Bulk parameterization of the snow field in a cloud model. *J. Climate Appl. Meteor.*, **22,** 1065–1092.

Riehl, H., and J. S. Malkus, 1958: On the heat balance in the equatorial trough zone. *Geophysica*, **6,** 503–535.

——, and J. Simpson, 1979: The heat balance of the equatorial trough zone, revisited. *Beitr. Phys. Atmos.*, **52,** 287–305.

Simpson, J., 1988: Tropical Rainfall Measuring Mission (TRMM): A satellite mission to measure Tropical rainfall. Report of the Science Steering Group, 94 pp. [Available from NASA Publications, Government Printing Office, Washington, DC 20402.]

——, R. F. Adler, and G. R. North, 1988: A proposed satellite tropical rainfall measuring mission (TRMM). *Bull. Amer. Meteor. Soc.*, **69,** 278–295.

Smith, P. L., 1984: Equivalent radar reflectivity factors for snow and ice particles. *J. Climate Appl. Meteor.*, **23,** 1258–1260.

Smith, P. L., Jr., C. G. Myers, and H. D. Orville, 1975: Radar reflectivity factor calculations in numerical cloud models using bulk parameterization of precipitation. *J. Appl. Meteor.*, **14,** 1156–1165.

Soong, S.-T., and W.-K. Tao, 1980: Response of deep tropical clouds to mesoscale processes. *J. Atmos. Sci.*, **37,** 2035–2050.

Steiner, M., and R. A. Houze Jr., 1993: Three-dimensional validation at TRMM ground truth sites: Some early results from Darwin, Australia. Preprints, *26th Int. Conf. on Radar Meteorology*, Norman, OK, Amer. Meteor. Soc., 417–423.

——, ——, and S. E. Yuter, 1995: Climatological characterization of three-dimensional storm structure from operational radar and rain gauge data. *J. Appl. Meteor.* **34,** 1978–2007.

Tao, W.-K., 1983: A numerical study of the structure and vertical transport properties of a tropical convective system. Ph. D. dissertation, University of Illinois, 228 pp. [Available from Dept. of Atmospheric Sciences, University of Illinois, 105 S. Gregory St., Urbana, IL 61801.]

——, and S.-T. Soong, 1986: A study of the response of deep tropical clouds to mesoscale processes: Three-dimensional numerical experiments. *J. Atmos. Sci.,* **43,** 2653–2676.

——, and J. Simpson, 1989: Modeling study of a tropical squall-type convective line. *J. Atmos. Sci.*, **46,** 177–202.

——, and ——, 1993: The Goddard Cumulus Ensemble Model. Part I: Model description. *Terr. Atmos. Oceanic Sci.,* **4,** 35–72.

——, ——, S. Lang, M. McCumber, R. Adler, and R. Penc, 1990: An algorithm to estimate the heating budget from vertical hydrometeor profiles. *J. Appl. Meteor.*, **29,** 1232–1244.

——, S. Lang, J. Simpson, and R. Adler, 1993: Retrieval algorithms for estimating the vertical profiles of latent heat release: Their applications for TRMM. *J. Meteor. Soc. Japan*, **71,** 685–700.

Witt, A., and J. T. Johnson, 1993: An enhanced storm cell identification and tracking algorithm. Preprints, *26th Int. Conf. on Radar Meteorology,* Norman, OK, Amer. Meteor. Soc., 417–423.

Yanai, M., S. Esbensen, and J. H. Chu, 1973: Determination of bulk properties of tropical cloud clusters from large-scale heat and moisture budgets. *J. Atmos. Sci.,* **30,** 611–627.